Science Advances
AAAS

advances.sciencemag.org/cgi/content/full/6/5/eaax1464/DC1

Supplementary Materials for

Complex multiphase organohydrogels with programmable mechanics toward adaptive soft-matter machines

Shuyun Zhuo, Ziguang Zhao, Zhexin Xie, Yufei Hao, Yichao Xu, Tianyi Zhao, Huanjun Li, Elias M. Knubben, Li Wen*, Lei Jiang, Mingjie Liu*

*Corresponding author. Email: liumj@buaa.edu.cn (M.L.); liwen@buaa.edu.cn (L.W.)

Published 31 January 2020, *Sci. Adv.* **6**, eaax1464 (2020)
DOI: 10.1126/sciadv.aax1464

The PDF file includes:

Other Supplementary Material for this manuscript includes the following:

(available at advances.sciencemag.org/cgi/content/full/6/5/eaax1464/DC1)

Section S1. Characterization of microstructure

The oil-in-water emulsion was characterized using an optical microscope (Nikon LV100N). The microstructures of the organohydrogel samples were characterized using a scanning electron microscopy (SEM, JEOL-7500 apparatus, at an accelerating voltage of 5 kV) and a confocal laser scanning microscopy (CLSM, Olympus FV1000-IX81 confocal laser biological microscope). For SEM measurements, the organohydrogel was dried for 0.5 h at room temperature. For CLSM measurements, the hydrogels were stained with the hydrophilic dyes (DAPI, blue), and the microrganogel domains were stained with the oleophilic dyes (Perylene Red, red). The morphology of Aluminum sol was characterized using transmission electron microscopy (TEM) (JEM-2100F).

Section S2. WAXS measurements and analysis

WAXS measurements were performed on Xeuss WAXS/SAXS system, France. The wavelength of the X-ray was 0.154 nm. Organogel samples with a thickness of 1 mm were set in the X-ray transmission direction, and the distance from samples to the detector was 116.5 mm with the acquisition time of 1200 s. The diffractograms were recorded over the range from 2 ° to 40 °, at different temperatures from 10° to 80°C.

WAXS curves of the triple-switching organohydrogel and its three oleophilic components were shown in fig. S3. The Bragg-peak positions of $C_{28}H_{58}$ at a low range (0 to 10°) were found to be at integral multiples of the fundamental peak (2.7° (d-spacing of 3.27 nm) and 5.5° (d-spacing of 1.68 nm)), indicating a periodic lamellar arrangement of molecular layers. The peaks at the range of 20-25° represented the triclinic geometry *(29)*. PSMA exhibited a crystalline peak at 22.2° corresponding to a Bragg d-spacing of 0.40 nm, which can be attributed to paraffin-like hexagonal lattices with interplanar spacing (100) formed by the long alkyl side chain of PSMA *(33, 34)*. A sharp peak at a low angle (2.9°) was apparent, corresponding to a lattice spacing of 3.04 nm. The peaks of $C_{16}H_{34}$ at 20.0°, 20.5°, 23.0° and 24.2° were characteristic peaks of triclinic (010), (011), (100), and (111), respectively *(30-32)*. All peaks appeared in WAXS curves of the organohydrogel, and no additional peaks showed in the whole range, indicating that each component remained its independent character and was not co-crystallized with each other. This was due to the differences in the crystal structure and crystallizing temperature, as well as weak interactions between the components, disfavoring the crystallization in a common lattice.

Section S3. Optical microscope measurements

The crystallization process was recorded by an optical microscope (Nikon LV100N). The organogel sample at melting state was placed between two cover slides with a gap of 0.1 mm. Measurements were conducted in the temperature range of 10° to 80°C.

Section S4. DSC measurements and analysis

DSC measurements were conducted on the PerkinElmer Pyris 1 TGA under nitrogen atmosphere. The gel samples sealed in aluminum pans were scanned between 0 and 85°C at a scanning rate of 10 °C/min.

The degree of crystallinity (χ_c) of each component was calculated by using the following equation

$$\chi_c\ \% = \Delta H' / \Delta H \times 100$$

where χ_c is the degree of crystallinity, ΔH, $\Delta H'$ is the melting and crystallization enthalpy per gram of the sample, which is obtained from the integral area of the baseline and each melting peak in DSC.

χ_cs for $C_{16}H_{34}$, PSMA, and $C_{28}H_{58}$ were 95.2%, 91.8%, and 96.3%, respectively, at heating/cooling rate of 10 °C/min. This result demonstrated the reversible crystallization/melting property of organohydrogels.

Section S5. Measurements of rheological properties

The rheological properties of the gel samples were investigated on an Anton Paar model MCR-301 rheometer. Organohydrogel samples in form of sheets (15 mm diameter × 2 mm height) were set under a 15 mm diameter parallel plate. Under a variety of temperatures, the storage moduli (G') of organohydrogels were swept at 15.8 rad s^{-1} and a constant strain (γ) of 0.1 %. In cyclic tests, the storage moduli were repeatedly measured through heating-cooling the organohydrogel samples (10°, 30°, 45°, and 65°C in sequence).

Section S6. Measurements of mechanical properties

The compression and tensile measurements of organohydrogels at varying temperatures were performed using a tensile-compressive tester with a 1000 N load cell (Tensilon HZ-1004D, Hengzhun Instrument Technology Co., China). In tensile test, cylinder-shaped (6 mm diameter × 30 mm height) samples were stretched at a strain rate of 10 mm min^{-1} up to a maximum strain ε_m. In compression tests, cylinder-shaped (6 mm diameter × 5 mm height) samples were measured at

a constant compression rate of 10 mm min^{-1}. Cyclic tests of compression modulus were carried out with 3 samples from 3 batches. In every single test, one original sample was compressed to 30% strain at different temperatures. Then the sample underwent heating-cooling cycles (10° -30° -45° -65° -45° -30° -10°C in sequence) for 49 times, after that the sample was tested again at 10°, 30°, 45°, and 65°C. The tensile modulus/compressive modulus was calculated from the linear slope of the stress-strain curves between 0-10 % stretch/compression.

Section S7. Infrared thermal imaging test of the soft robots

The real-time temperature of organohydrogel-based grippers and tentacles under electrical stimuli was measured and recorded using an infrared thermometer (FLUKE Ti32, IR fusion technology). For the organohydrogel-based soft finger, 14 V, 18 V, and 22 V were applied for specific temperatures. For the organohydrogel-based sucker, a step-shaped voltage was applied: first, a slightly higher voltage was used to heat the sucker to the required temperature; then a lower voltage was applied to stabilize the temperature.

Section S8. Measurements of self-healing capacity

Self-healing behaviors of the organohydrogels were carried out in two methods.

In first part, we cut gel sample or finger actuator into two parts and then kept the cut surfaces in contact. Finally, the broken sample healed in a sealed container at $T>T_m$ (80°C) for 2 hours in air. External force was used to bring the cut surfaces contacting with each other and was removed during the self-healing process. Tensile tests were conducted on original and healed samples, and self-healing efficiency was evaluated by using the following equation

$$H_e = \varepsilon'/\varepsilon \times 100,\ H_s = R_m'/R_m \times 100,\ H_m = E'/E \times 100$$

where ε', R_m', and E' are the strain at break, tensile strength and tensile modulus of the self-healed sample; ε, R_m, and E are the strain at break, tensile strength and tensile modulus of the original sample;

In addition, the airtightness of the organohydrogel-based actuator shell was examined through actuating the finger till the bending angle up to 90 °.

In second part, organohydrogel film was scratched on the surface with the fracture gap ~50μm. The damaged film healed in sealed containers at 80°C for 30 minutes in air. The details of the scratches were recorded using an optical microscope (Nikon LV100N). Furthermore, the

organohydrogel-based finger was damaged with an obvious scratch at the tip, then healed in sealed containers at 80°C for 2 hours in air. After that, actuation-deactuation cyclic measurement was conducted to test the self-healing effect.

Section S9. Measurements of the pull-off force of grippers

Six-axis force transducer (Mini 40 F/T sensor, ATI, America) was used to test the pull-off force of the grippers. A cylinder (diameter 3 cm, fixed on test-bed) was fixed and connected to the force transducer. The gripper composed of two fingers grasped the cylinder and was pulled off vertically at a constant speed of 20 mm min^{-1} under various electrical stimuli. A consistent pressure of 25 kPa was used in this test and the pull-off force was defined as the maximum force generated by the gripper in the whole grasping-detaching process.

Section S10. Measurements of the controllable grasping performance of grippers

The plasticines with the different modulus (0.24 and 0.62 MPa) in size of 30 mm (length) ×10 mm (width) × 2 mm (height) were placed on the pressure transducer (Mini 40 F/T sensor, ATI, America). The organohydrogel-based gripper with microstructures (cylinder pillar array) on the back was put on the top of the plasticine. A constant grasping force of 1 N was applied on the plasticine for 30 s at different modulus of the gripper through controlling temperature. The grasping force was controlled using an electrical universal material testing machine with a 500 N load cell (EZ-Test, SHIMADZU). The surface of the plasticine during the grasping process was recorded by a camera.

Section S11. Measurements of the actuation-deactuation cycles of organohydrogel-based soft finger

The soft finger was actuated at 0.33 Hz, 30 kPa at 35°C and 21 kPa at 70°C. The bending angles were recorded by a camera. The test was carried out in silicone oil.

Section S12. Sucker attachment force test

In this section, we detailed a single gel sucker attachment force measurement. We investigated the engagement of suckers on four flat surfaces of different roughness (R_a= 0, 20, 50, 200μm). We described the prototypes used in the experiments and the experimental setup.

Experimental substrates: Four substrate surfaces (roughness R_a= 0, 20, 50, 200μm) were used in this study. To control for the effects of material stiffness, wettability, surface chemistry, and temperature, and to focus on the effect of surface roughness on adhesion, the surfaces were fabricated with the same epoxy resin material (EpoxAcast 650, Smooth-On Inc., PA, USA).

We first created the substrate surface of around 20μm roughness. A female die was made from Dragonskin 20 as a cast of corresponding sandpaper (FEPA Grit designation P600, corresponding to an average particle diameter of 21μm). Next, casting epoxy was poured into the female die, allowed to cure for 24 hours, and removed from the die. Then the same procedure was used to create the other two substrate surfaces with the roughness of around 50μm and 200μm (respectively with FEPA Grit designation P240 and P80 sandpaper, corresponding to an average particle diameter of 51μm and 201μm). The smooth flat substrate surface with a nanometer-scale roughness was created with a mold made from glass. The four flat substrates were fastened to a 3D-printed plastic base plate fixed on the testing machine

Experimental setup for measuring sucker attachment force: The sucker attachment force for the gel sucker was measured using an electrical universal material testing machine with a 500 N load cell (EZ-Test, SHIMADZU). The prepared experimental substrates were fixed on the test machine, and the single organohydrogel-based sucker was clamped on the pulling level of the testing machine. The sucker was initially adjusted with the pulling level to attached the experimental substrate, a vacuum pressure of -60 kPa was applied to the sucker to achieve full attachment to the substrate. After that, the sucker was pulled off with a constant velocity of 50 mm min^{-1} by the pulling level until the attach failure occurred. Tests with the organohydrogel-based sucker electrified under voltages from 0 V to 17 V were conducted on all the four substrates (R_a= 0, 20, 50, 200μm), for each test, five trials were conducted to produce an error measurement.

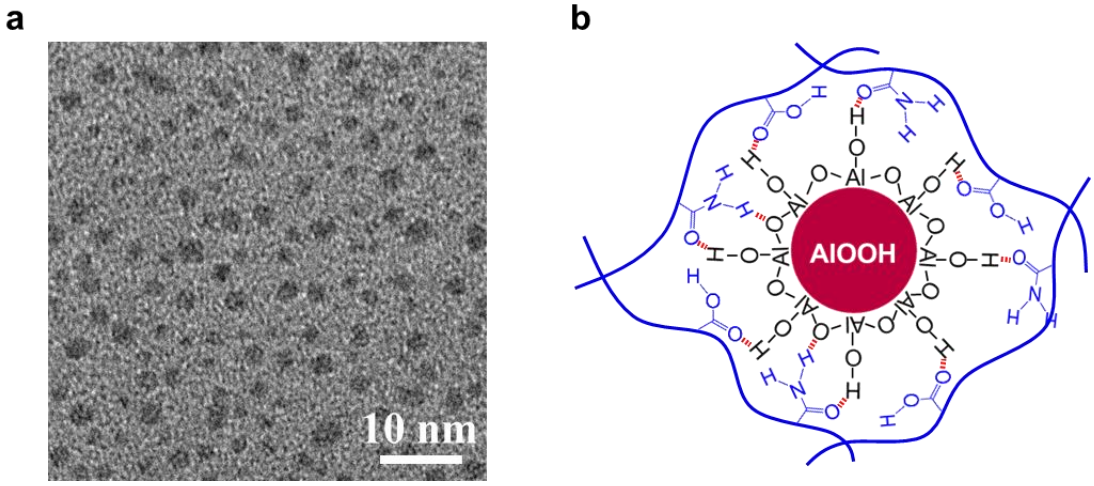

Fig. S1. Characterization and illustration of ANPs. (**A**) TEM image of AlOOH nanoparticles (ANPs). Scale bar, 10 nm. (**B**) Schematic of physical crosslinking between ANPs and hydrogel polymer chains.

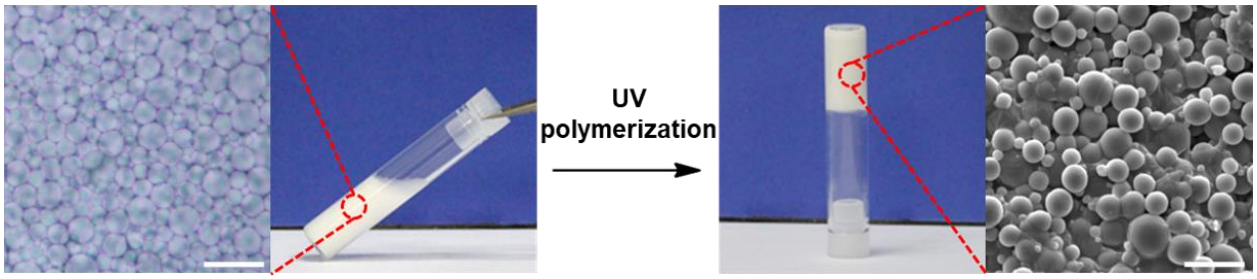

Fig. S2. Images of the preparation of the organohydrogels by UV photoinitiated in situ polymerization. Optical microscope image and the digital photograph of the oil-in-water emulsion (left), digital photograph and SEM image of the organohydrogel (right). Scale bar, 5μm. (Photo credit: Shuyun Zhuo and Ziguang Zhao, Beihang University).

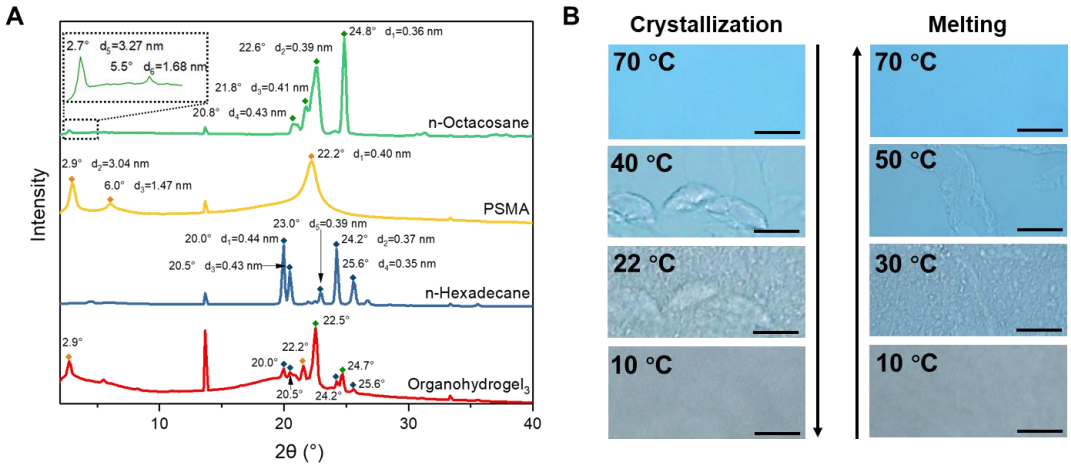

Fig. S3. Crystallization-melting property of triple-switching organohydrogels. (A) WAXS spectrum of organohydrogels and three components of the microrganogel inclusions. (B) Optical microscope images of the organogel showing varying transmittance at different temperatures. Scale bar, 100μm.

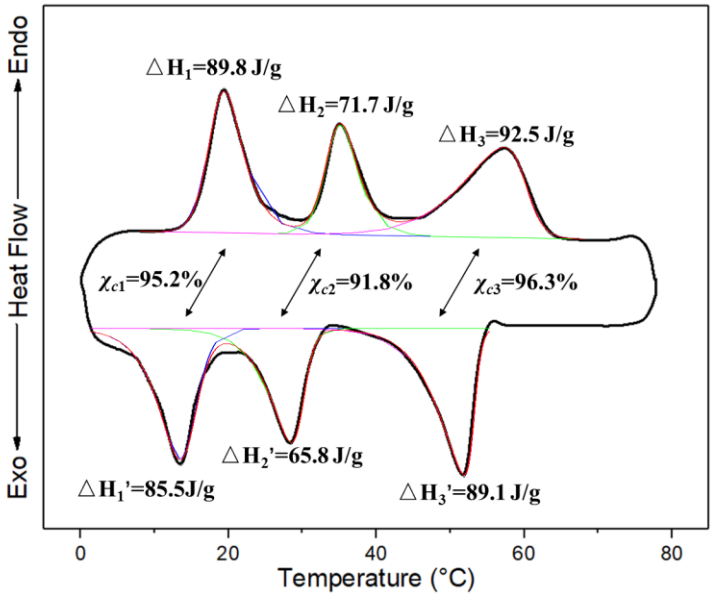

Fig. S4. The crystallization/melting enthalpy and crystallinity (χ_c) of triple-switching organohydrogel.

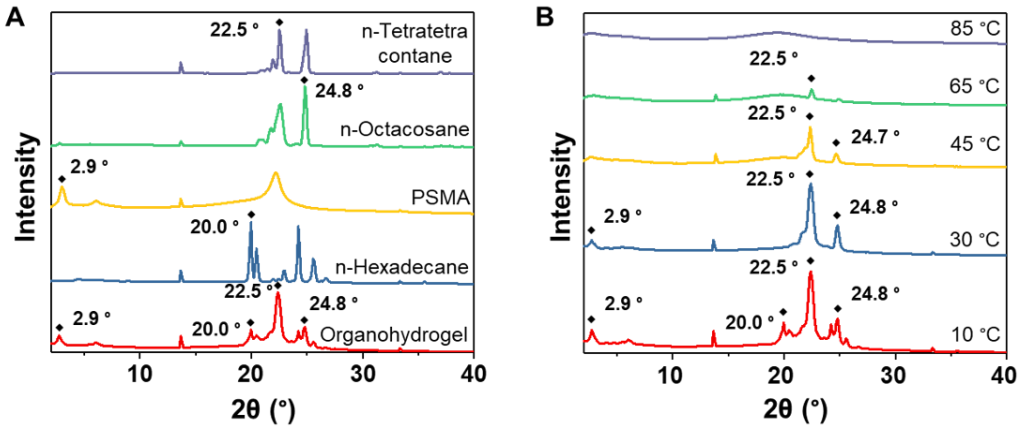

Fig. S5. WAXS spectrum of quadruple-switching organohydrogel. (A) WAXS spectrum of organohydrogel and its four components inside the microrganogel inclusions. (B) WAXS spectrum of organohydrogels at different temperatures.

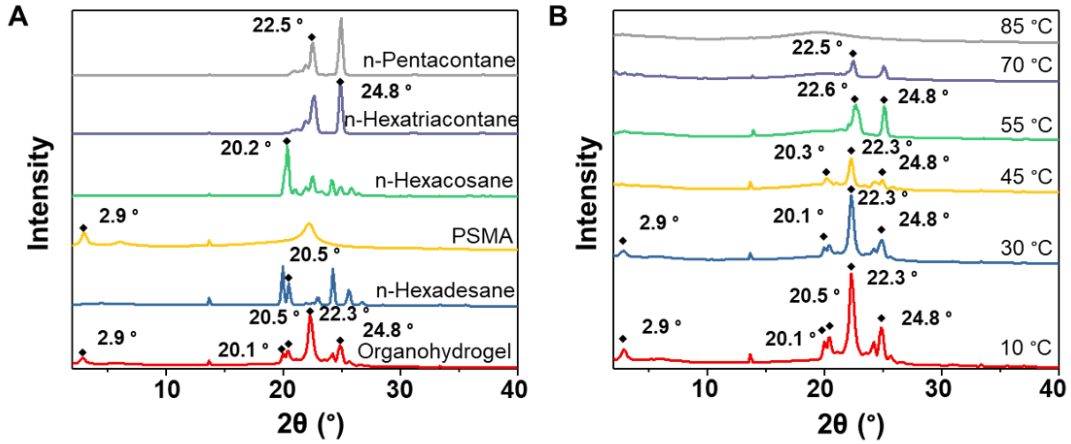

Fig. S6. WAXS spectrum of quintuple-switching organohydrogel. (**A**) WAXS spectrum of organohydrogel and its five components inside the microrganogel inclusions. (**B**) WAXS spectrum of organohydrogel at different temperatures.

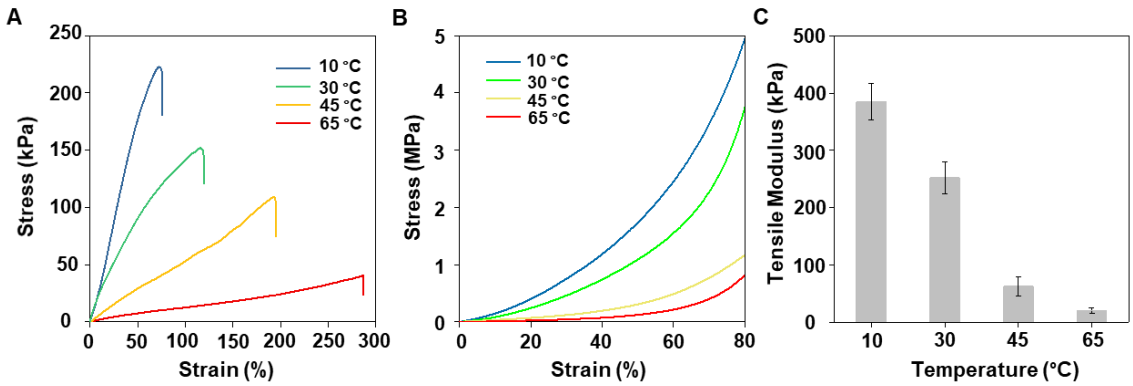

Fig. S7. Mechanical properties of triple-switching organohydrogels at different temperatures. (**A**) tensile strain-stress curves, (**B**) compressive strain-stress curves, and (**C**) tensile modulus. The error bars represent one standard deviation (n =6).

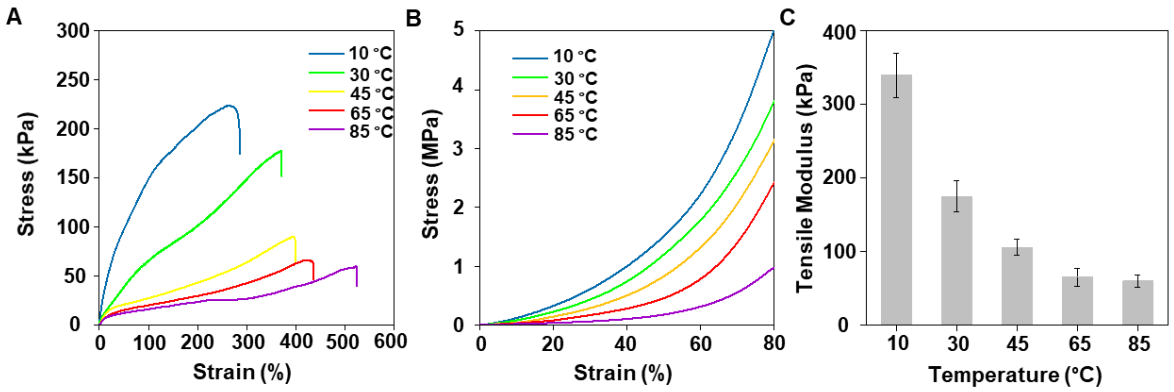

Fig. S8. Mechanical properties of quadruple-switching organohydrogel at different temperatures. (**A**) tensile strain-stress curves, (**B**) compressive strain-stress curves, and (**C**) tensile modulus. The error bars represent one standard deviation (n =6).

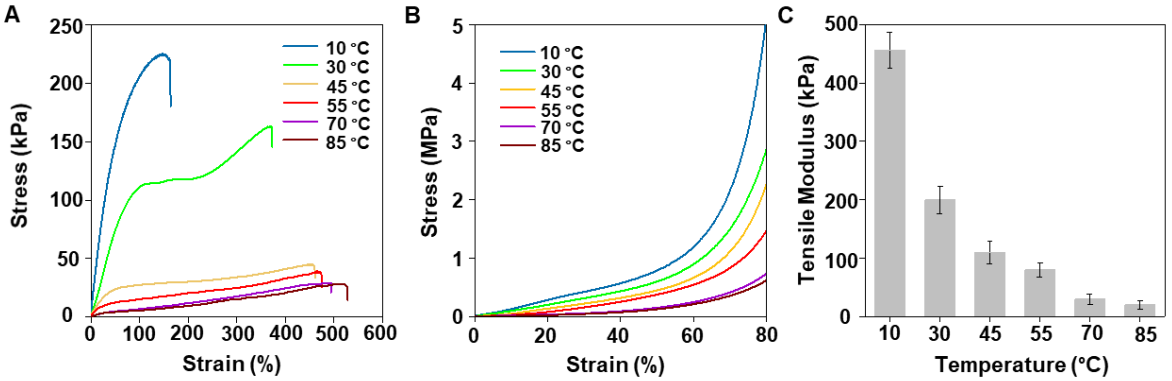

Fig. S9. Mechanical properties of quintuple-switching organohydrogels at different temperatures. (**A**) tensile strain-stress curves, (**B**) compressive strain-stress curves, and (**C**) tensile modulus. The error bars represent one standard deviation (n =6).

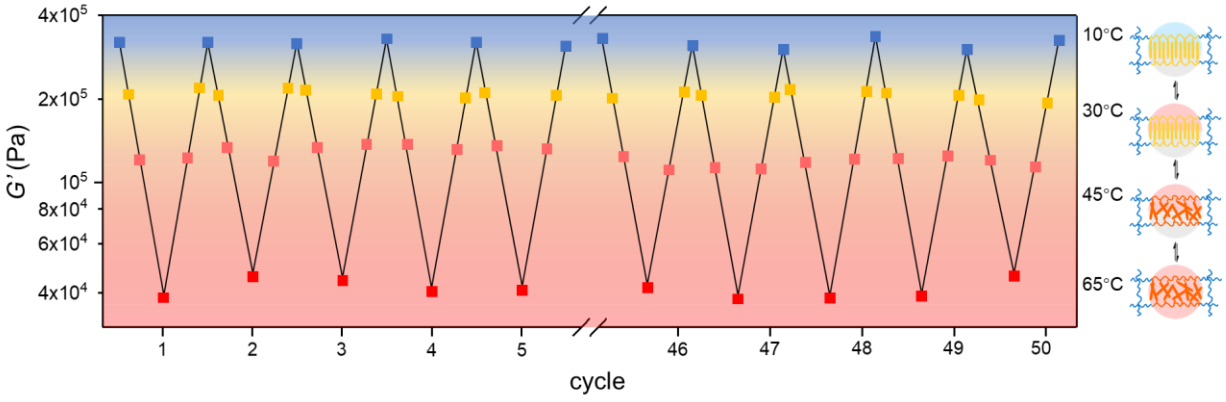

Fig. S10. Modulus of the organohydrogel at different temperatures during crystallization-melting cycles.

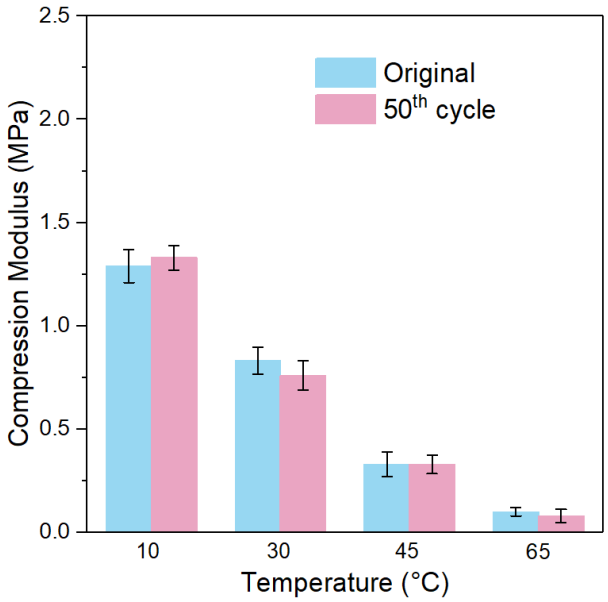

Fig. S11. Compression modulus of the organohydrogel material at original state and on the 50th crystallization-melting cycle [df = 1, *F* = 0.01, and *P* = 0.975, analysis of variance (ANOVA)]. The error bars represent one standard deviation (n =3).

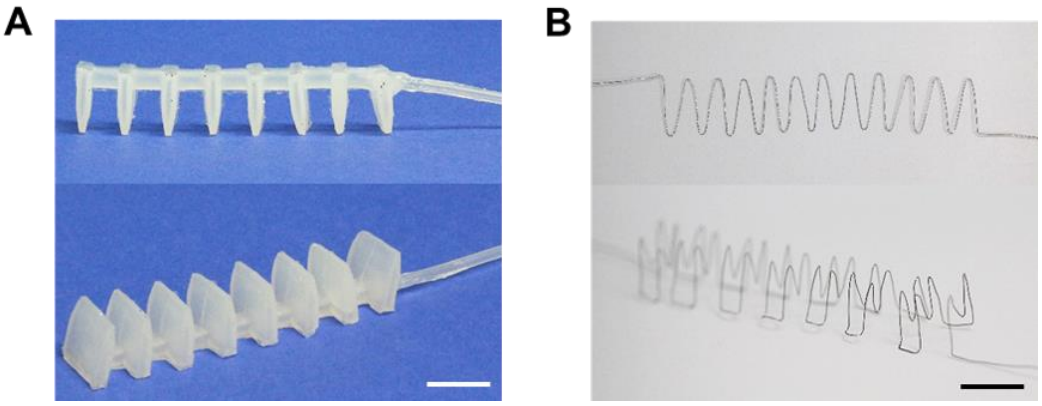

Fig. S12. Images of the grippers' components. (**A**) the silicone gas-cell with an air duct and (**B**) Ni–Cr resistive wire with a diameter of 0.1 mm. Scale bar, 1cm. (Photo credit: Shuyun Zhuo, Beihang University).

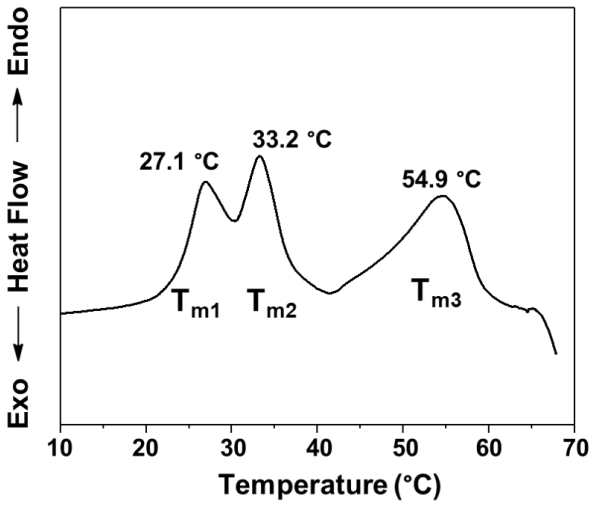

Fig. S13. DSC curve of the organohydrogel materials for soft-matter machines. The independent phase transition performance indicates the triple-switching mechanics of the resulting gel materials.

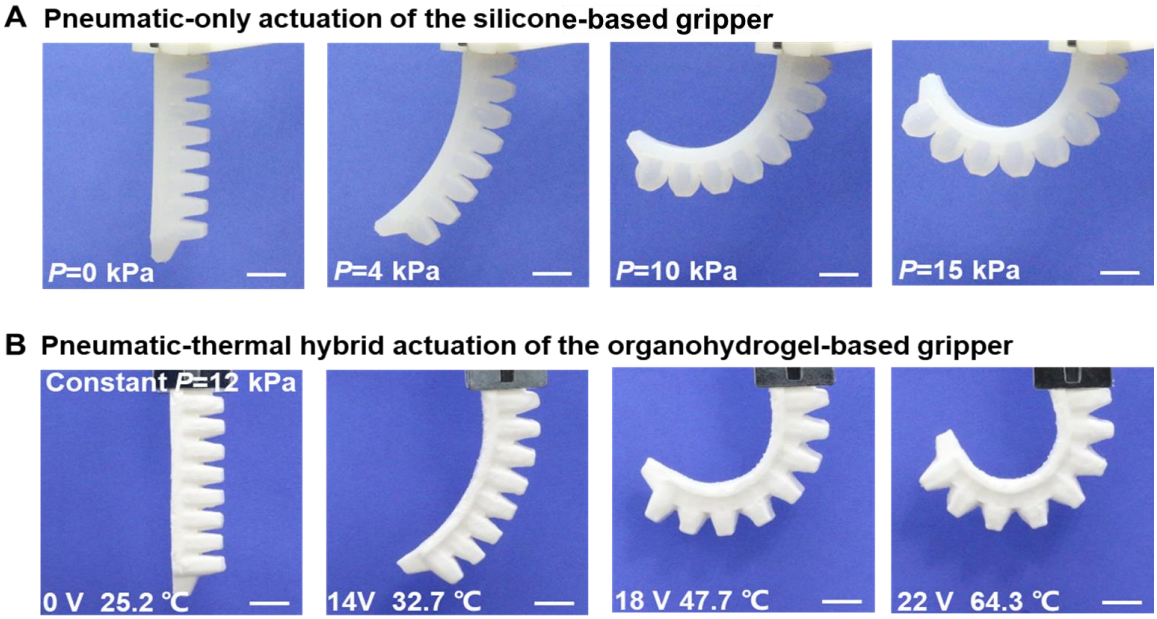

Fig. S14. The actuation process of the traditional silicone-based gripper and organohydrogel-based gripper. (**A**) Pneumatic-only actuation of the silicone-based gripper depends on the regulation of the pressure, high pressure with large bending angles. (**B**) Pneumatic-thermal hybrid actuation of the organohydrogel-based gripper through tuning the mechanical properties under electrical stimuli at a consistent pressure of 12 kPa. Scale bar, 1cm. (Photo credit: Shuyun Zhuo and Yufei Hao, Beihang University).

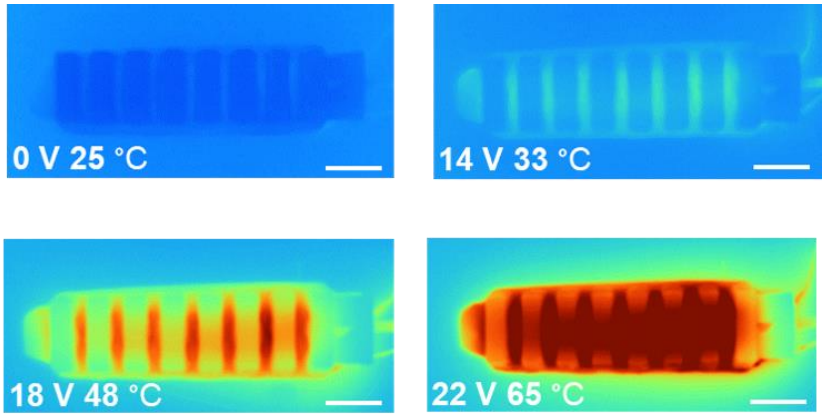

Fig. S15. Infrared images of the gripper from the top view showing its increased temperature by powered at different voltages. The current increased to 140mA (14V), 200mA (18V) and 220mA (22V) and the electric power is calculated to be 1.96W, 3.60W and 4.84W, respectively. Scale bar, 1 cm.

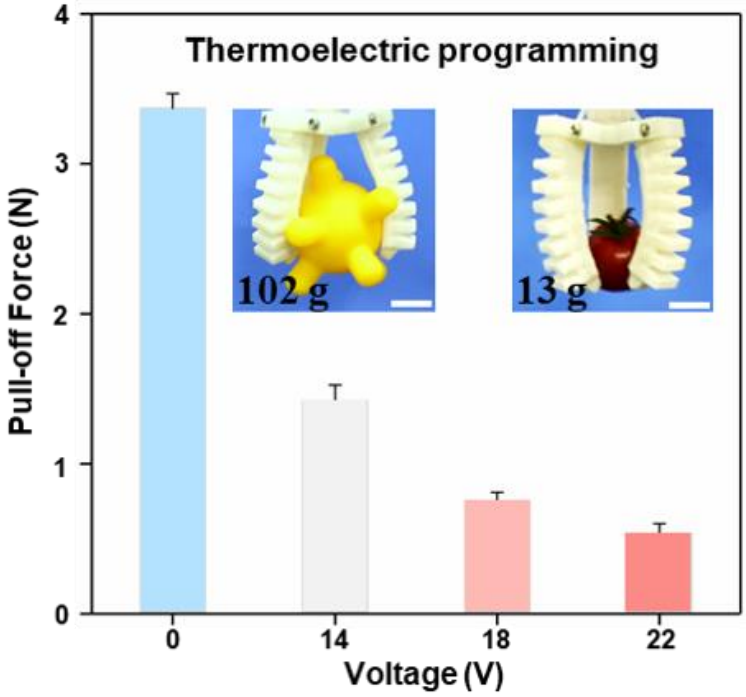

Fig. S16. The pull-off force of a single gripper at different voltages under constant pressure (25 kPa). The inset photos show the gripper can grasp objects with varied weights. The error bars represent one standard deviation (n =6). (Photo credit: Shuyun Zhuo and Yufei Hao, Beihang University).

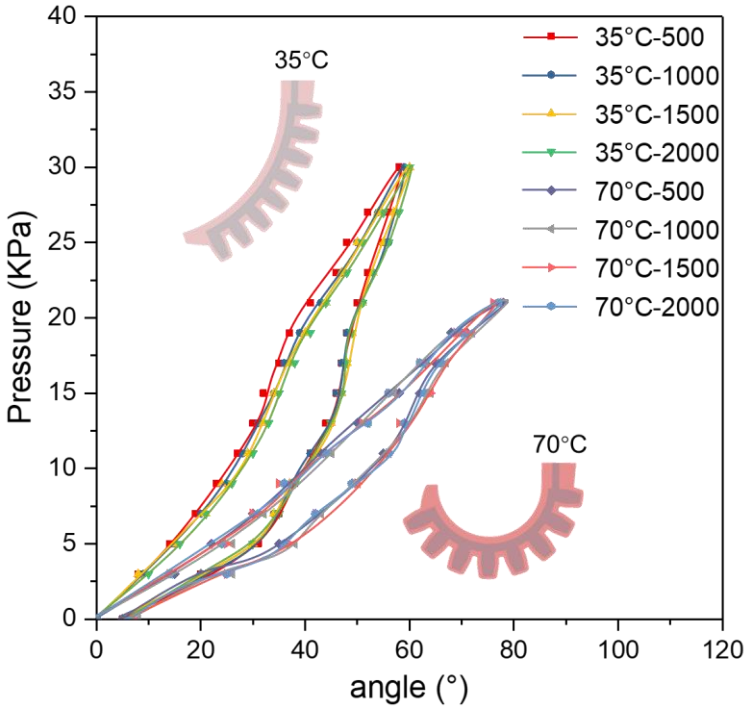

Fig. S17. Pressure (*P*)–bending angle (*α*) curves of actuation-deactuation cycles of the soft finger at different temperatures.

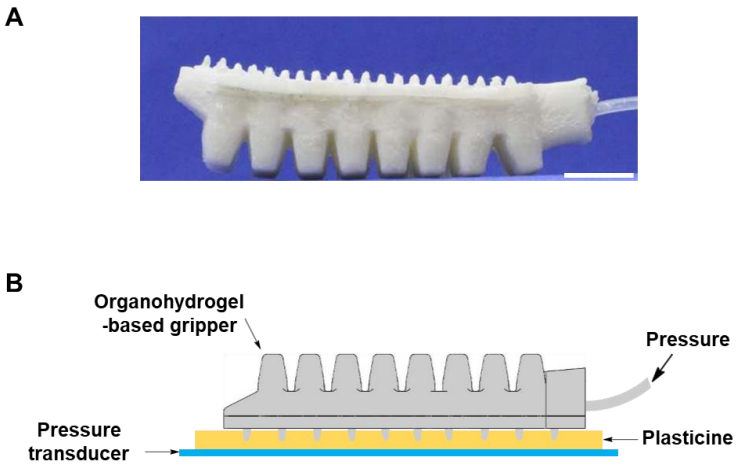

Fig. S18. Schematic of the structured organohydrogel-based soft gripper. (**A**) Photo of the gripper with microstructures (pillars) on the back. Scale bar, 1 cm. (**B**) Illustration of the measurement of the gripper's adaptive grasping performance. (Photo credit: Shuyun Zhuo and Ziguang Zhao, Beihang University).

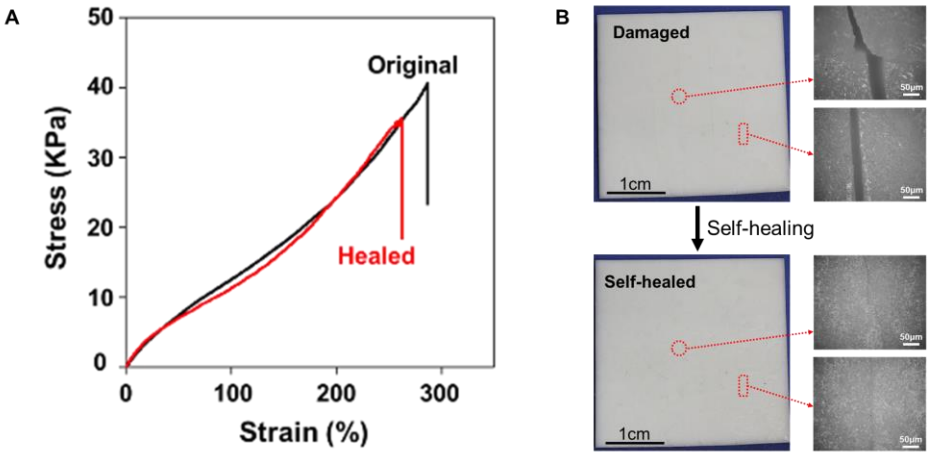

Fig. S19. Self-healing property of the organohydrogel. (A) Strain-stress curves of the original and healed samples at 65 °C. **(B)** Self-healing process of the organohydrogel. Digital photos showing the damaged and self-healed organohydrogels; optical microscope photos showing the details of the fracture surfaces. (Photo credit: Shuyun Zhuo, Beihang University).

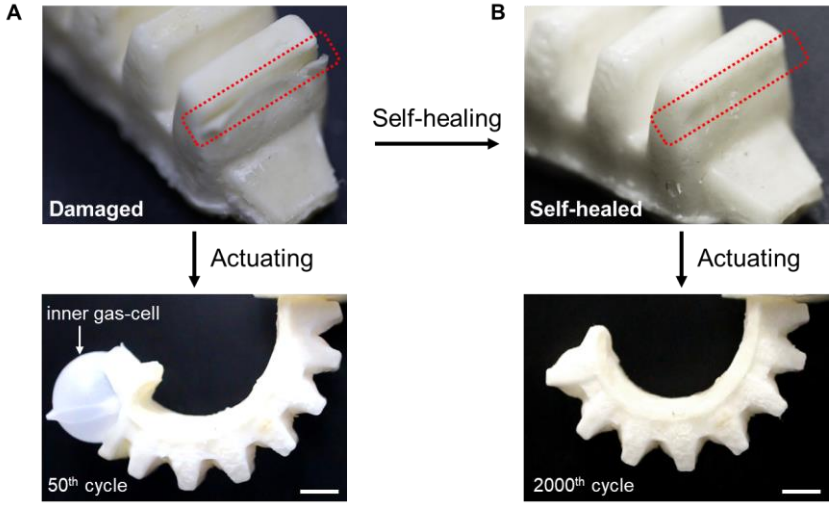

Fig. S20. The influence of self-healing property on the soft finger' working life span. (A) without healing, the broken finger loses working capability at 50th actuation-deactuation cycles; (B) the healed finger gains working capability and can be repeatedly operated for more than 2000 cycles. Scale bar, 1 cm. (Photo credit: Shuyun Zhuo and Zhexin Xie, Beihang University).

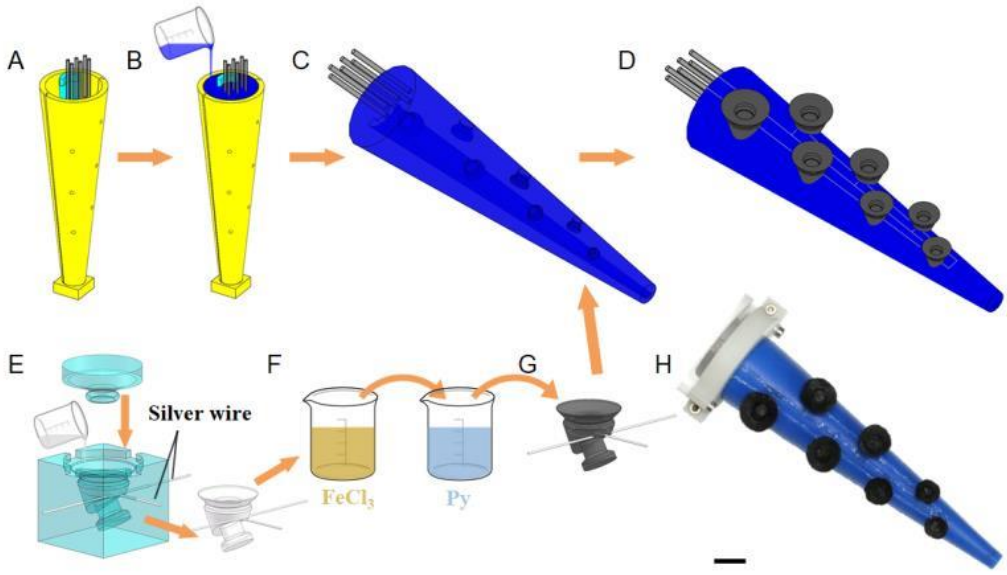

Fig. S21. Fabrication of the octopus-inspired tentacles. (**A-G**) The fabrication process and (**H**) optical image of the octopus-inspired tentacles.

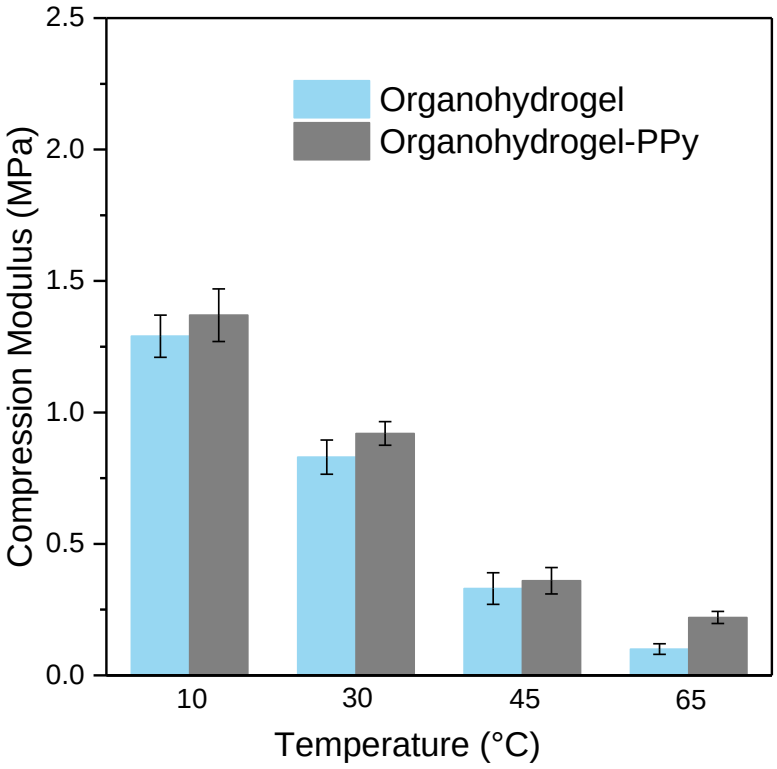

Fig. S22. Compression modulus of organohydrogel and organohydrogel PPy at different temperatures. The error bars represent one standard deviation (n = 6).

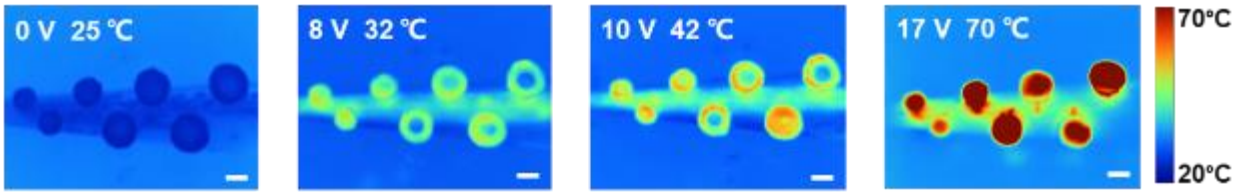

Fig. S23. Infrared images of the octopus-inspired tentacle at different voltages. The current increased to 15mA (14V), 32mA (18V) and 63mA (22V) and the electric power is calculated to be 0.21W, 0.58W and 1.39W, respectively. Scale bar, 1 cm.

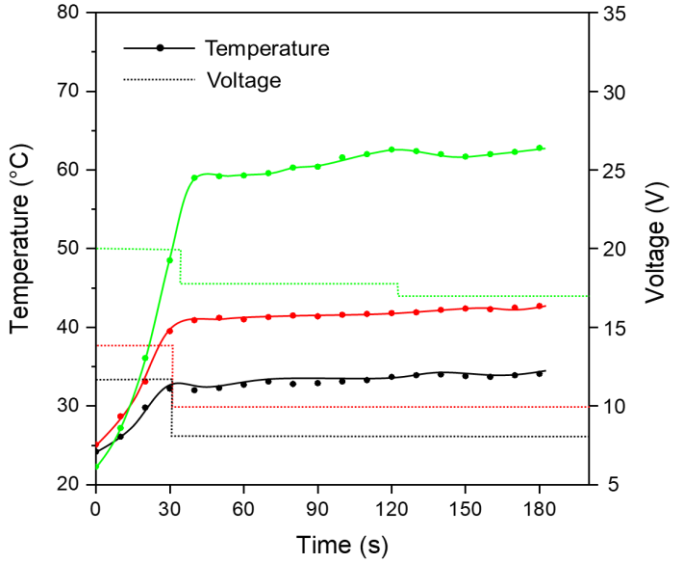

Fig. S24. The temperature-time relationship of the organohydrogel-based soft robots under different voltages.

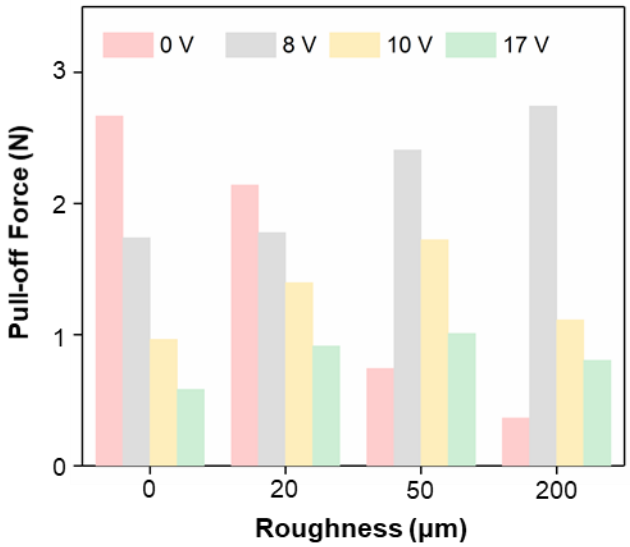

Fig. S25. The pull-off force of a single sucker on the surfaces with different roughnesses under varied electrical stimuli.

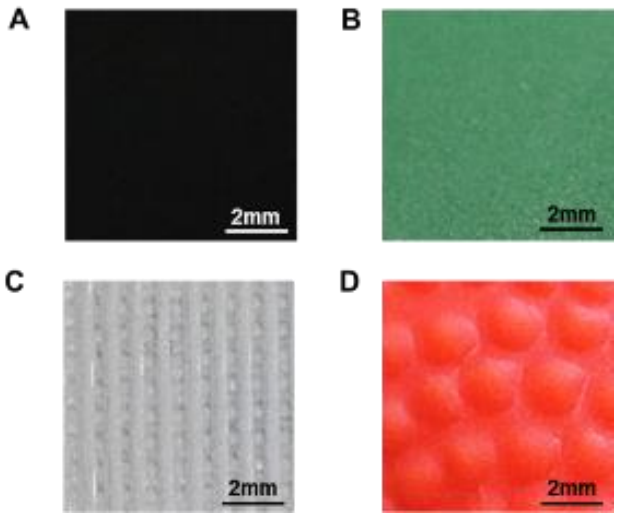

Fig. S26. Photos from the top view of different surfaces. (**A**) a phone. (**B**) a smooth ball. (**C**) a rough resin box and (**D**) a toy basketball. Scale bar, 2 mm. (Photo credit: Shuyun Zhuo and Zhexin Xie, Beihang University).

Table S1. Mechanical characteristics of triple-switching organohydrogels at different temperatures.

Temperature (°C)	Elongation (%)	Tensile strength (kPa)	Tensile modulus (kPa)	Compression strength (MPa)	Compression modulus (MPa)
10	75.91±13.25	222.69±18.19	384.52±32.13	4.95±0.42	1.29±0.08
30	118.89±16.74	152.10±16.21	252.19±28.41	3.75±0.26	0.83±0.07
45	194.71±20.58	109.27±13.88	62.44±16.20	1.17±0.13	0.33±0.06
65	286.73±22.36	40.48±10.54	20.13±5.14	0.81±0.05	0.10±0.02

The error bars represent one standard deviation (n = 6).

Table S2. Mechanical characteristics of quadruple-switching organohydrogels at different temperatures.

Temperature (°C)	Elongation (%)	Tensile strength (kPa)	Tensile modulus (kPa)	Compression strength (MPa)	Compression modulus (MPa)
10	281.54±30.21	223.15±20.86	340.68±30.12	5.03±0.55	1.43±0.08
30	369.63±24.19	177.61±19.10	175.44±21.64	3.80±0.39	0.96±0.05
45	399.58±33.79	89.97±12.44	106.37±11.25	3.14±0.52	0.44±0.03
65	430.39±29.31	62.38±10.59	65.89±12.14	2.42±0.27	0.32±0.04
85	523.14±28.75	55.72±9.13	60.04±8.10	0.97±0.11	0.17±0.02

The error bars represent one standard deviation (n = 6).

Table S3. Mechanical characteristics of quintuple-switching organohydrogels at different temperatures.

Temperature (°C)	Elongation (%)	Tensile strength (kPa)	Tensile modulus (kPa)	Compression strength (MPa)	Compression modulus (MPa)
10	163.24±25.18	220.51±23.54	456.45±31.21	5.01±0.62	1.25±0.07
30	365.18±30.27	161.83±26.10	200.79±23.87	2.84±0.22	0.94±0.05
45	468.97±38.55	52.30±18.64	110.44±19.53	2.25±0.14	0.45±0.06
55	481.32±20.46	36.54±11.83	80.76±12.45	1.45±0.07	0.25±0.07
70	495.45±35.21	28.11±8.76	30.08±8.64	0.72±0.11	0.14±0.03
85	526.87±27.16	27.35±7.91	20.50±6.71	0.55±0.09	0.06±0.02

The error bars represent one standard deviation (n = 6).

Table S4. Mechanical characteristics of the original and self-healed organohydrogels.

Samples	Elongation (%)	H_e (%)	Tensile strength (kPa)	H_s (%)	Tensile Modulus (kPa)	H_m (%)
Original samples	287.13		40.66		20.01	
Self-healed sample 1	263.62	91.81	36.41	89.55	21.35	100
Self-healed sample 2	252.46	87.93	38.10	93.70	18.72	93.55
Self-healed sample 3	275.10	95.81	35.91	88.32	19.87	99.30
Self-healed sample 4	255.21	88.89	37.42	92.03	20.34	100
Self-healed sample 5	260.58	90.75	36.24	89.13	20.16	100

Movie S1. Pneumatic-thermal hybrid actuation of the organohydrogel-based soft gripper.

Movie S2. Repeated heating-actuating-cooling cycles of the soft gripper.

Movie S3. Adaptive grasping performance of the soft gripper.

Movie S4. Protective grasping through matching the modulus of the soft gripper and the object.

Movie S5. Adhesion on and grasping a phone on the smooth flat surface.

Movie S6. Adhesion on and grasping a rubber ball on the smooth curved surface.

Movie S7. Programmable adhesion on the rough flat surface of a resin box.

Movie S8. Programmable adhesion on the rough curved surface of a basketball.